# 7 Silicon Carbide Crystals — Part II: Process Physics and Modeling

Q.-S. Chen[1], V. Prasad[3], H. Zhang[1], and M. Dudley[2]

Center for Crystal Growth Research, [1]Department of Mechanical Engineering, [2]Department of Materials Science and Engineering, State University of New York at Stony Brook, Stony Brook, NY 11794-2200
[3]College of Engineering, Florida International University, Miami, FL 33174

## Nomenclature

| | |
|---|---|
| $a$ | activity |
| $A$ | area ($m^2$) |
| $\boldsymbol{A}$ | magnetic vector potential (Wb/m) |
| $A_{SiC}$ | growth area ($m^2$) |
| $\boldsymbol{B}$ | magnetic flux density (T) |
| $c_p$ | isobaric specific heat, (J/kg/K) |
| $d_p$ | mean diameter of the charge particles (m) |
| $D$ | diffusion coefficient ($m^2/s$) |
| $D_c$ | diameter of crucible (m) |
| $f$ | frequency (Hz) |
| $F$ | radiation view factor |
| $g$ | gravitational acceleration ($m/s^2$) |
| $Gr$ | Grashof number, $\rho^2 g \beta R^3 \Delta T/\mu^2$ |
| $G_{SiC}$ | growth rate (m/s), dissolving rate of particles (m/s) |
| $\Delta G_T^0$ | isobaric-isothermal Gibbs-function |
| $h$ | heat transfer coefficient ($W/m^2/K$) |
| $\Delta h_{f,298}^0$ | heat of formation |
| $H$ | latent heat (J/kg) |
| $I$ | current (A) |
| $\boldsymbol{J}$ | current density ($A/m^2$) |
| $k$ | thermal conductivity (W/m/K) |
| $K$ | equilibrium constant of a chemical reaction |
| $L$ | gap between the charge and seed (m) |
| $M$ | molecular weight (kg/mol) |
| $p$ | pressure (Pa) |
| $P$ | partial pressure (Pa) |
| $Pe$ | mass Pélet number ($UL/D$) |

| | |
|---|---|
| $Pr$ | Prandtl number ($\mu c_p/k$) |
| $q$ | heat flux (W/m$^2$) |
| $q'''_{eddy}$ | heat generated by eddy currents (W/m$^3$) |
| $q''_{radi}$ | radiative heat flux (W/m$^2$) |
| $Q$ | heat flux (W) |
| $r$ | radial coordinate (m) |
| $R$ | universal gas constant, 8.314 (J/mol/K); heat resistance (K/W) |
| $R_s$ | radius of susceptor (m) |
| $Ra$ | Rayleigh number ($Gr \cdot Pr$) |
| $t$ | time (s) |
| $T$ | temperature (K) |
| $\Delta T$ | temperature difference between the charge and seed (K) |
| $u$ | displacement component |
| $U$ | advective velocity (m/s), activation energy (J/mol) |
| $v$ | displacement component |
| $z$ | axial coordinate (m) |

## Greek Symbol

| | |
|---|---|
| $\alpha$ | absorptivity, thermal expansion coefficient, sticking coefficient |
| $\beta$ | volumetric expansion coefficient (1/K) |
| $\varepsilon$ | emissivity, strain |
| $\varepsilon_m$ | permittivity ($F$/m) |
| $\varepsilon_p$ | porosity of SiC charge |
| $\mu$ | viscosity (kg/m/s) |
| $\mu_m$ | magnetic permeability ($H$/m) |
| $\rho$ | density (kg/m$^3$) |
| $\rho_c$ | density of crystal (kg/m$^3$) |
| $\sigma_c$ | electrical conductivity (1/$\Omega$/m) |
| $\sigma$ | Stefan-Boltzmann constant $5.670 \times 10^{-8}$ (W/m$^2$/K$^4$), stress |
| $\omega$ | angular frequency (rad/s) |

## Subscripts

| | |
|---|---|
| $\infty$ | ambient |
| *boun* | boundary |
| *coil* | induction coil |
| *cond* | conductive |
| *conv* | convective |
| *eddy* | eddy current |
| *eff* | effective |
| *gas* | gas |
| *insu* | insulation material |

| | |
|---|---|
| *radi* | radiative |
| *real* | real part of a complex quantity |
| *s* | solid |
| *Ste* | Stefan |
| $\theta$ | angular direction |

## 7.1 Introduction

Silicon carbide crystals of 50–100 mm diameter are now commercially grown using the method of physical vapor transport, commonly known as the modified Lely method. A detailed review of the historical development of SiC growth, micropipes and other defects in as-grown crystals, issues and challenges of the current process technology, and characteristics of the present industrial growth systems is presented in a companion article (Chapter 6) by Dhanaraj et al. [1]. Any advancement in crystal growth technology in terms of the boule size (diameter and length) and defect density strongly depends on the understanding of the process physics, better design of the growth system and effective control of the growth process. Since direct measurement of temperature, flow, species concentration, and growth rate is extremely difficult, if not impossible, physics-based modeling is the only way that one can develop an understanding of the transport mechanisms in a SiC growth system. The models can also help in process optimization and system design.

Modeling and simulation of SiC crystal growth has attracted significant research interests in last five years or so, and growth models have been developed by several investigators, namely, Hofmann et al. [2,3], Pons et al. [4,5], Egorov et al. [6], Müller et al. [7,8], Karpov et al. [9], Chen and co-workers [10–15], Selder et al. [16], and Räback et al. [17–19]. Various degrees of system complexity have been considered by these authors, such as electromagnetic field produced by RF heating, generated heat power in the graphite susceptor, conduction and radiation heat transfer, temperature distribution, and growth kinetics.

Hofmann et al. [2,3] modeled the temperature distributions for a growth temperature of 2573 K and system pressure of up to 3500 Pa. Pons et al. [4,5] calculated the electromagnetic field and temperature distribution, and found that the predicted temperatures for the seed and powder surface (2920 K and 3020 K) are much larger than the external temperatures measured at the top and bottom of the crucible (2390 K and 2500 K), while the maximum temperature of the insulation foam on its periphery is about 1000 K. The total pressure is around 30 Torr (4000 Pa) and the growth rate is 1.55 mm/h. Egorov et al. [6] modeled the global heat transfer inside the system for SiC growth in a tantalum container. Müller et al. [7,8] calculated the temperature distributions in inductively heated SiC growth reactors at temperatures of 2373–2673 K, and found that the temperatures in the powder are highly nonuniform, and predicted radial variations of 30–50 K along the powder surface. Karpov et al. [9] predicted growth rate in the growth of SiC in a tantalum container.

Ma et al. [10] performed an order-of-magnitude analysis of parameters in the SiC PVT growth, and used a one-dimensional network model and two-dimensional finite-volume model to predict the temperature distribution in a 75 mm growth system. Chen and co-workers [11–15] proposed a kinetics model for SiC vapor growth, predicted growth rate as a function of temperature, temperature gradient, and inert gas pressure, and obtained a growth rate profile across the seed surface from the temperature distribution in a 75 mm growth system. The powder charge is modeled as a solid matrix with a porosity and an effective conductivity that accounts for both the conduction and radiation in the powder.

Selder et al. [16] introduced a modeling approach for the simulation of heat and mass transfer during SiC bulk crystal growth and compared calculated results with the experimental data. Räback et al. [17–19] presented a model for the growth rate of the SiC sublimation process and estimated the parametric dependencies of the growth rate.

## 7.2 Modeling of Heat and Mass Transfer and Growth Rate

### 7.2.1 Growth process

A typical SiC growth system consists of an RF copper coil, quartz tube, graphite susceptor, graphite insulation, crucible, and some other components (Fig. 7.1). The graphite crucible is filled with a SiC powder charge, and a SiC seed is placed on the bottom of the lid of the crucible as shown in Fig. 7.1. The seed is cooled by heat loss through the top hole. The SiC powder charge is heated by RF induction heating that is generated by passing through the coil a radio-frequency current. The current required depends on the number of turns of coil and distance between the coil and the susceptor. The time-harmonic electromagnetic field induces eddy currents in the graphite susceptor that has a high electrical conductivity, and heat is generated in a thin (skin) layer of the susceptor. Sometimes a double-walled water-cooled quartz tube is used to seal the system [5,20,21] that enables us to reduce the thickness of the insulation, and enhance the coupling between the coil and the susceptor. The system is maintained at a very low pressure using a vacuum pump, and an argon container is linked to the end plate to control the pressure inside the quartz tube and create an inert gas environment. Two holes are bored in the graphite insulation above and below the crucible to monitor the temperatures of the seed and the charge using pyrometers. The temperature inside the top hole is controlled, which is lower than the seed temperature.

The growth process consists of several steps [22,23]: (a) *vacuum degassing stage*—a low gas pressure ($10^{-3}$ Pa) and an evacuation temperature of 1073 K < $T$ < 1273 K are applied to reduce the background nitrogen contamination; (b) *preheating stage*—temperature is gradually increased in high-purity argon environment (about $10^5$ Pa) to the growth temperature and stabilized to achieve an optimum $\Delta T$ between the source and the seed; (c) *growth stage*—a programmed

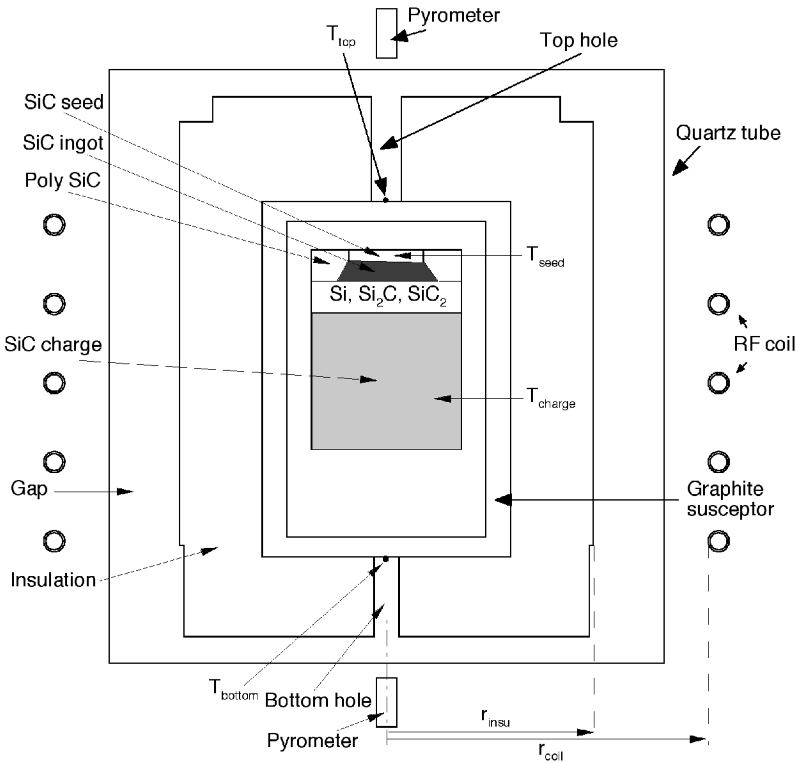


**Fig. 7.1.** Schematic of an RF-heated furnace for the growth of single SiC crystals by PVT

pressure reduction is used to achieve low-defect nucleation and uniform epitaxy on the oriented seed crystal, and argon pressure is decreased to $10 < p < 2.66 \times 10^4$ Pa, and boule growth begins; and (d) *cooling stage*—the temperature is reduced. The temperature difference between the charge and the seed during the growth stage depends on the system configuration. According to Lilov [24], SiC dissociates completely into liquid silicon and solid carbon at $T > 3150$ K and therefore the growth temperature must lie below 3150 K. Various growth systems used by industry employ different growth temperatures depending on the temperature gradient in the growth chamber; a higher growth temperature is usually associated with a lower temperature gradient and a higher pressure. Although a model can account for various stages of the growth as outlined above, those reported in the literature have thus far primarily focused on step (c), the growth stage.

### 7.2.2 Flow and heat transfer parameters

The flow in a silicon carbide growth system is induced by: (a) the buoyancy force that is produced by the variations in temperature on crucible walls, and (b) the ad-

vection due to sublimation of SiC charge. The flow is essential to bring the SiC vapor and other species from the charge at the bottom to the growth surface at the top. The effect of buoyancy can be determined by the Grashof number,

$$Gr = \frac{\rho^2 g\beta D_c^{\ 3}\Delta T}{\mu^2} = \frac{\rho^2 g D_c^{\ 3}}{\mu^2}\frac{\Delta T}{T}, \tag{7.1}$$

where the isobaric expansion coefficient, $\beta = -\frac{1}{\rho}\frac{\partial\rho}{\partial T} = \frac{1}{T}$, if the argon-vapor mixture is considered as an ideal gas, and the Prandtl number,

$$Pr = \frac{\mu c_p}{k} \tag{7.2}$$

For a typical process condition of $3 \times 10^4$ Pa as the system pressure, 2900 K as the growth temperature, 30 K as the temperature difference ($\Delta T$), the Prandtl number is obtained as 0.66 while the Grashof number is estimated to be 3 and 24 for crucible (inner) diameters of 50 mm and 100 mm, respectively. These values of the Grashof number are far below the threshold at which natural convection can be considered appreciable [4,10]. Even though in the case of a cylinder heated on the outer wall natural convection can occur at any Rayleigh number, $Ra$ must be above 1707 for the onset of convection in an enclosure heated from below and cooled at the top (Bénard convection). The present configuration does not conform to any of these two classical cases. It is still reasonable to consider that buoyancy flow plays a far less important role than radiative and conductive heat transfer in a SiC growth system. However, in the next generation systems for large diameter SiC crystal growth, the Grashof number may not remain this small. For example, if the crucible (inner) height becomes 500 mm, $Gr$ based on height will increase to about 3000 leading to appreciable buoyancy effects. Even though $Gr = 3000$ is not very large, the complex temperature boundary conditions can lead to complex flows, a combination of Bénard convection and vertical boundary layer flows. For such convective flow analysis, a model based on fluid-superposed porous layer theory as outlined by Prasad [25] and Chen et al. [26,27] can be used.

The Stefan flow on the other hand is caused by volumetric expansion of silicon carbide species due to dissolving and sublimation of the charge. The species mainly include gaseous Si, $Si_2C$, $SiC_2$, and SiC. The partial pressure of each species in the charge reaches an equilibrium value, which is a strong function of temperature. The transport of species from the charge to seed is determined by the Stefan flow and growth kinetics. The Stefan flow is therefore very important for mass transfer and growth rate.

If leakage and diffusion are neglected, the advective velocity of SiC vapor flow can be estimated from,

$$U = \rho_{SiC} G_{SiC} A_{SiC} / \alpha \rho_{gas} A_{gas}, \tag{7.3}$$

where the vapor density is $\rho_{gas} = pM/RT$, $A_{SiC}$ is the growth area, and $\alpha$ is the sticking coefficient. This leads to the mass Péclet number,

$$Pe = UL/D, \tag{7.4}$$

where the diffusion coefficient can be obtained from $D = D_0(T/T_0)^n\ (p_0/p)$ [28], with $D_0 = 5 \times 10^{-6} \sim 2 \times 10^{-4}$ m$^2$/s, n = 1.8, $T_0 = 273$ K, and $p_0 = 1$ atm. Using $D_0 = 5 \times 10^{-6} \sim 1 \times 10^{-5}$ m$^2$/s and $L = 50$ mm, Chen et al. [13] have calculated the advective velocity, diffusion coefficient, density, and Péclet number for two operating conditions, one with a low growth temperature and low gas pressure and another with a high growth temperature and high gas pressure (Table 7.1).

If the buoyancy effects are neglected, the heat transfer in the SiC growth system will depend on the latent heat released during the deposition (or absorbed during the sublimation), heat transfer by Stefan flow (advective mass transport), and radiative heat transfer inside the growth system. These three heat transfer quantities can be estimated from,

$$Q_{latent} = \rho_{SiC}\, G_{SiC}\, A_{SiC}\, \Delta H_{vs}, \tag{7.5a}$$

$$Q_{Stefan} = \rho_{SiC}\, G_{SiC}\, A_{SiC}\, c_p \Delta T, \tag{7.5b}$$

$$Q_{radi} = \varepsilon A_{SiC}\, \sigma \left(T_{charge}^4 - T_{seed}^4\right) \tag{7.5c}$$

For a growth rate of $G_{SiC} = 1$ mm/h, a diameter of 50 mm, $\Delta T = 30$ K, $\varepsilon = 0.8$, and $T_{seed} = 2900$ K, $Q_{latent}$, $Q_{Stefan}$, and $Q_{radi}$ are estimated to be 0.01 W, 0.1 W, and 1000 W, respectively. It is therefore reasonable to neglect the latent heat released and heat transfer by Stefan flow while calculating the temperature distribution. It should, however, be noted that the temperature distribution inside the crucible will depend on the temperature conditions on the inner surfaces of the crucible and conduction and radiation in the SiC charge. As shown later, these heat transfer mechanisms can be easily included in a physics-based mathematical model for the system. Another important issue to keep in mind is the effect of latent heat release on the growth phenomena since a small change in temperature gradient (due to condensation) in the vicinity of the growth interface can significantly affect the growth behaviors. It has also been commonly assumed that the chemical reaction, both exothermic and endothermic, does not contribute much to the heat transfer and temperature distribution [4].

**Table 7.1.** Advective flow parameters for two different operating conditions [13]

| | U [m/s] | D [m$^2$/s] | ρ [kg/m$^3$] | α | Pe |
|---|---|---|---|---|---|
| 2600 K, 20 Torr (2666 Pa) | 0.178 | $2.16 \times 10^{-2}$ | $4.92 \times 10^{-3}$ | 1 | 0.41 |
| 2900 K, 200 Torr (26,666 Pa) | 0.0199 | $3.98 \times 10^{-4}$ | $4.41 \times 10^{-2}$ | 1 | 2.5 |

### 7.2.3 One-dimensional network model

As a first approximation, a heat resistance network analysis can be very useful in developing a basic understanding of the thermal behavior of a SiC growth system [10]. In the absence of convective heat transfer, the thermal field in a SiC growth system is dominated by the interplay of conduction and radiation within and between the different components.

A typical SiC system, as shown schematically in Fig. 7.2(a), can be easily represented by a heat resistance network (Fig. 7.2b). For this simple analysis, the inner surfaces of the upper and lower graphite susceptors can be treated at fixed temperatures, $T_a$ and $T_b$. The heat resistances for conduction, convection, and radiation are given by

$$R_{cond} = \frac{L}{kA}, \qquad R_{conv} = \frac{1}{hA}, \tag{7.6a, b}$$

$$R_{radi} = \frac{1}{\varepsilon\sigma(T_1 + T_2)(T_1^2 + T_2^2)A} \approx \frac{1}{4\varepsilon\sigma T_{av}^3 A}, \tag{7.6c}$$

where $L$ is the thickness, $k$ is the thermal conductivity, $A$ is the area, $h$ is the heat transfer coefficient, $\varepsilon$ is emissivity, $\sigma$ is the Stefan-Boltzmann constant, and $T_{av}$ is the average temperature of two surfaces under consideration, $T_{av} = \frac{T_1+T_2}{2}$, where $T_1$ and $T_2$ are the temperatures of the two surfaces.

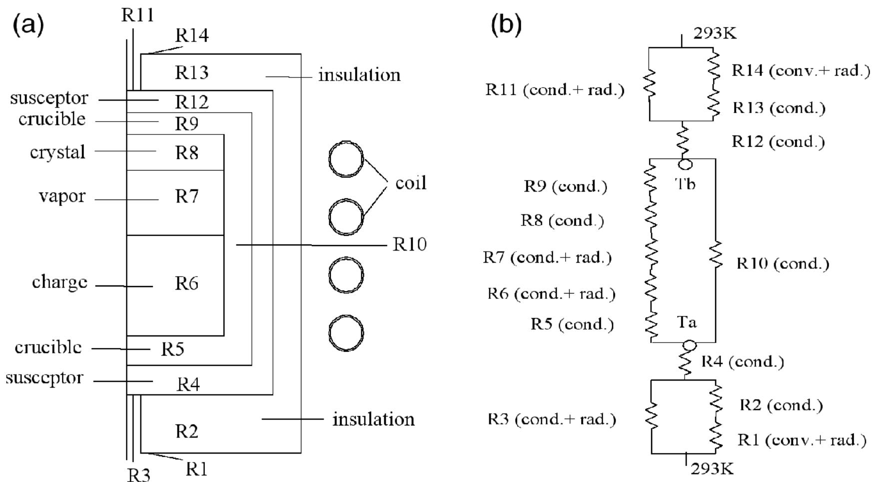


**Fig. 7.2.** (a) Schematic and (b) thermal network of a SiC growth system (cond. — conduction, conv. — convection, rad. — radiation) [10]

It is necessary to consider both conduction and radiation from particle to particle to account for the heat transfer within the SiC charge. Several correlations for

the effective heat transfer coefficient due to radiation in a porous matrix have been reported in the literature [29]. One of these correlations valid for spherical particles is given by Kansa et al. [30],

$$h_{radi,\,porous} = \frac{8}{3}\varepsilon\varepsilon_p \sigma 4 T_{av}{}^3 d_p, \tag{7.7}$$

where $\varepsilon_p$ is the porosity for a randomly packed spherical bed, $T_{av}$ is the average temperature of the charge, and $d_p$ is the average particle diameter.

Figure 7.2(b) shows the thermal network diagram for a typical SiC growth system using the electrical circuit analogy. The resistances in various components of a typical growth system have been calculated by Ma et al. [10], which give a good indication of the magnitude of heat transfer through various components.

### 7.2.4 Thermal transport model

In developing a thermal transport model for SiC growth, it is important to consider the electromagnetic field generated by RF heating, heat generation, conduction and radiation in various parts of the growth system, and appropriate boundary conditions. The effects of convective heat transfer as discussed in Section 7.2.2 have been neglected by almost all investigators thus far. However, they may need to be considered as the PVT growth system is upscaled. A short discription of the major components of the model is given below.

#### *Calculation of electromagnetic field*

The electromagnetic field produced by an RF induction coil can be calculated by using Maxwell equations, and the generated heat power in the graphite susceptor can be predicted by low frequency eddy current theory ($f < 1$ MHz). For the present problem, the Maxwell equations can be simplified using the quasi-steady approximation. It is commonly assumed that the current in the coil is time-harmonic, and heat in the graphite susceptor is generated only by eddy currents [31]. Under such conditions, the magnetic flux density can be expressed as the curl of a magnetic potential vector, $\mathbf{B} = \nabla \times \mathbf{A}$, and the Maxwell equations can be written in terms of the vector potential, $\boldsymbol{A}$, as,

$$\nabla \times \left(\frac{1}{\mu_m}\nabla \times \mathbf{A}\right) + \varepsilon_m \frac{\partial^2 \mathbf{A}}{\partial t^2} + \sigma_c \frac{\partial \mathbf{A}}{\partial t} = \mathbf{J}_{coil} \tag{7.8}$$

Assuming that the coil and the electromagnetic field are axi-symmetric, such that both $\boldsymbol{A}$ and the current density, $\mathbf{J}_{coil}$, have only one angular component each with an exponential form,

$$\mathbf{A} = \begin{Bmatrix} 0 \\ A_0 e^{i\omega t} + cc \\ 0 \end{Bmatrix}, \quad \text{and} \quad \mathbf{J}_{coil} = \begin{Bmatrix} 0 \\ J_0 e^{i\omega t} + cc \\ 0 \end{Bmatrix}, \tag{7.9}$$

where $i$ is the complex unit, and $cc$ denotes the complex conjugate. The final equation for **A** is obtained by substituting Eqs. (7.9) in Eq. (7.8),

$$\left(\frac{\partial^2}{\partial r^2}+\frac{1}{r}\frac{\partial}{\partial r}-\frac{1}{r^2}+\frac{\partial^2}{\partial z^2}\right)\left(\frac{A_0}{\mu_m}\right)+\varepsilon_m\,\omega^2 A_0 - i\omega\sigma_c A_0 = -J_0 \tag{7.10}$$

In an axisymmetric system, the following boundary conditions can be used to solve equation (7.10),

$$A_0 = 0, \qquad \text{at } r = 0, \text{ and } (r^2 + z^2) \rightarrow \infty \tag{7.11}$$

After solving equations (7.10) for $A_0$, the generated heat power by eddy currents in the graphite susceptor can be obtained from [31,32],

$$q'''_{eddy} = \frac{1}{2}\sigma_c\,\omega^2 A_0 A_0^{*} \tag{7.12}$$

where * denotes the complex conjugate. Further details of the electromagnetic field formulation can be found in Bíró and Preis [31], Pons et al. [4] and Chen et al. [13].

### *Energy transport*

In the absence of convective flows, temperature distribution in the growth system can be calculated using an energy transport equation,

$$(\rho c_p)_{eff}\frac{\partial T}{\partial t} = \nabla\cdot(k_{eff}\nabla T) + q'''_{eddy} - (q''_{radi} + q''_{insu})\,\delta A/\delta V, \tag{7.13}$$

where $q''_{radi}$ is the radiative heat flux normal to the inner surface of the radiation enclosure, and $\delta A$ and $\delta V$ are the area over a finite-volume face and finite volume near the gas/solid interface (see Fig. 7.3a), respectively. In Eq. (7.13), $q''_{insu}$ is the radiative heat flux on the outer surface of the insulation,

$$q''_{insu} = \varepsilon_{eff}\,\sigma(T^4 - T_\infty^{\,4}), \tag{7.14}$$

where $\varepsilon_{eff}$ is effective emissivity. For surfaces exposed to the ambient air, the effective emissivity can be chosen as that of the material, $\varepsilon_{eff} = \varepsilon_{insu}$. On the other hand, for surfaces exposed to the copper coil, the effective emissivity can be calculated from [33],

$$\varepsilon_{eff} = \frac{1}{1/\varepsilon_{insu} + r_{insu}/r_{coil}\,(1/\varepsilon_{coil} - 1)}, \tag{7.15}$$

so that the reflection of energy by the inner surface of the copper coil can be included in the formulation [13]. Here $\varepsilon_{insu}$ and $\varepsilon_{coil}$ are the emissivities of graphite insulation and copper coil, respectively, and $r_{insu}$ and $r_{coil}$ are the radii of the outer surface of insulation and inner surface of coil (as shown in Fig. 7.1).

Suitable boundary conditions must be used to solve Eq. (7.13). The computational domain for the energy equation is set as inside the quartz tube (Fig. 7.1), and the temperature on the quartz tube is set as 293 K. If it can be assumed that the three-dimensional effects are negligible, the symmetric condition

$$\frac{\partial T}{\partial r} = 0, \qquad \text{at} \quad r = 0 \tag{7.16}$$

can be used at the central axis. This condition is certainly applicable for good quality, slow growth as is evident from the symmetric growth striations reported in the literature (Selder et al., [16]). However, three-dimensional effects can become important if the growth system becomes larger, the material uniformity cannot be maintained, and/or there are fluctuations in power supply.

The thermal properties of various components (i.e., graphite susceptor, graphite insulation, crucible, and SiC charge) in the growth system should be considered as a function of temperature. Although most of the modeling studies consider SiC charge as a solid, Chen et al. [11,13] have considered the porosity of the charge and radiation from particle-to-particle. The effective heat capacity of the SiC powder charge can be estimated using the mixture theory,

$$(\rho c_p)_{eff} = (1 - \varepsilon_p)(\rho c_p)_{SiC} + \varepsilon_p (\rho c_p)_{gas}, \tag{7.17}$$

whereas the thermal conductivity can be obtained by considering the conduction-radiation heat transfer among the particles [30],

$$k_{eff} = (1 - \varepsilon_p) k_{SiC} + \varepsilon_p (k_{gas} + \frac{8}{3} \varepsilon \sigma 4 T^3 d_p) \tag{7.18}$$

Many other correlations for $k_{eff}$ can be found in Kaviany [29].

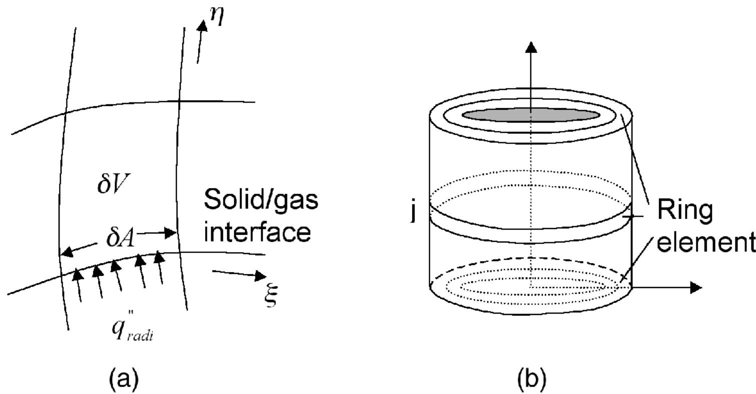


**Fig. 7.3.** (a) Heat flux on the radiation surface and curvilinear grid system, and (b) schematic of ring elements on radiative surfaces. The ring elements coincide with the finite volume grids for conduction calculation [13].

### *Radiative heat transfer*

Radiation is the dominant mode of heat transfer inside the crucible and requires special attention while developing a model for the SiC growth.

Pons et al. [4] have not considered the wall-to-wall radiation in the gas region, but assumed an apparent conductivity, greatly simplifying the energy equation [13] in their model. On the other hand, Hoffman et al. [2], Egorov et al. [6], and Chen and co-workers [13] have considered grid-to-grid gray-diffuse radiation together with appropriate view factors. This approach requires that all radiation surfaces be divided into grids and radiation view factors between each pair of these grids be calculated. In two-dimensional calculations, this, however, reduces to circular rings as shown in Fig. 7.3(b). It is also important that radiation heat transfer is calculated not only in the growth chamber but also in the bottom and top holes, as emphasized by Chen et al. [13].

Here, we describe the radiation model as adopted by Chen and co-workers [13], which is based on the method of discrete exchange factors (DEF) [34–36]. It is assumed that the radiation surfaces are gray, diffusely emitting and reflecting, and opaque. The radiation surface is broken into a number of rings each with uniform properties, and view factors between each pair of rings are calculated using appropriate relations [37]. The absorptivity $\alpha_j$ is assumed to be equal to the emissivity $\varepsilon_j$ in each ring. The integral equation for radiative heat transfer is then obtained as [33],

$$\frac{q''_{radi\,j}}{\varepsilon_j} - \sum_{k=1}^{N} F_{j,k} \frac{1-\varepsilon_k}{\varepsilon_k} q''_{radi\,k} = \sigma T_j^4 - \sum_{k=1}^{N} F_{j,k} \sigma T_k^4 \tag{7.19}$$

where $F_{j,k}$ is the view factor from ring $j$ to ring $k$ [37]. The above equations can be solved numerically by writing,

$$(A_{jk}) \cdot (q''_{radi\,k}) = (B_{jk}) \cdot (\sigma T_k^4), \tag{7.20}$$

where $A_{jk} = \frac{\delta_{jk}}{\varepsilon_k} - F_{j,k}\frac{1-\varepsilon_k}{\varepsilon_k}$, $B_{jk} = \delta_{jk} - F_{j,k}$, and $\delta_{j,k}$ is Kronecker's delta. The radiative heat flux can be written in the tensor form as,

$$q''_{radi\,j} = (\mathbf{A}^{-1} \cdot \mathbf{B})_{jk} \cdot (\sigma T_k^4) \tag{7.21}$$

The radiative heat flux is used as a source term in each computational element when solving the energy equation (7.13).

It should be noted that the spectral (wavelength dependence) behavior of radiation heat transfer is not accounted for in the above model although the radiative properties of SiC surfaces may be spectral. Secondly, the decomposition of SiC and accumulation/deposition of carbon particles can change the radiative properties inside the crucible significantly as the growth proceeds. Finally, the chemical species in the gas/vapor region may also participate in heat transfer by volumetric radiation. Since nothing is known of the participating behavior of any species other than carbon, this is a difficult task at present.

### 7.2.5 Mass transport model

Once the temperature field inside the crucible is obtained, a mass transport model can be used to calculate the distribution of species in the system. Hofmann et al.

[2], Pons et al. [4], and Chen et al. [11–14] have all considered the transport of species with various degrees of complexity. Since sublimation of SiC particles is associated with decomposition in various species and chemical reactions, a thermodynamic analysis is necessary for the calculations of partial pressures and species transport.

### *Equilibrium processes*

Mass spectrometric investigations conducted by Drowart and De Maria [38] have shown that the basic components of the evaporation of SiC are Si, $Si_2C$, $SiC_2$, and SiC. The content of the other components of evaporation ($Si_2$, C, $C_2$, $C_3$) in the vapor is insignificant and can be neglected. The following reactions are considered [38,24]:

$$SiC_{(s)} \Leftrightarrow Si_{(l)} + C_{(s)}, \quad K_1 = a_{Si} \tag{7.22}$$

$$SiC_{(s)} \Leftrightarrow Si_{(g)} + C_{(s)}, \quad K_2 = P_{Si} \tag{7.23}$$

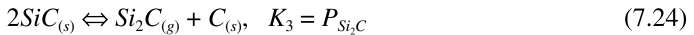

$$2SiC_{(s)} \Leftrightarrow Si_2C_{(g)} + C_{(s)}, \quad K_3 = P_{Si_2C} \tag{7.24}$$

$$2SiC_{(s)} \Leftrightarrow SiC_{2(g)} + Si_{(l,g)}, \quad K_4 = P_{SiC_2}\, P_{Si} \tag{7.25}$$

$$SiC_{(s)} \Leftrightarrow SiC_{(g)}. \quad K_5 = P_{SiC} \tag{7.26}$$

The equilibrium constant of a chemical reaction can be calculated from,

$$K_i = \exp(-\Delta G_T^0 / RT). \tag{7.27}$$

The change in isobaric-isothermal Gibbs-function $\Delta G_T^0$ for the reaction is given by,

$$\Delta G_T^0 = \sum_{prod} \nu_i (\Delta h_{f,298}^0 + h_T - h_{298} - Ts_T^0) - \sum_{reac} \nu_i (\Delta h_{f,298}^0 + h_T - h_{298} - Ts_T^0), \tag{7.28}$$

where $\Delta h_{f,298}^0$ is the heat of formation, $v_i$ is the stoichiometric coefficient, and $h_T$ is the enthalpy of the reacting species.

Lilov [24] has conducted a thermodynamic study on the partial pressure of each species. Up to 2546 K the pressure of silicon vapor above the silicon carbide is determined only by reaction (7.23) because the pressure of silicon ensured by (7.25) is less than the pressure of Si due to reaction (7.23). Therefore, in the temperature interval of 1500–2546 K, both reactions (7.23) and (7.25) take place simultaneously and the partial pressures of Si and $SiC_2$ are determined by, $P_{Si} = K_2$, $P_{SiC_2} = K_4 / P_{Si}$, respectively. In Table 7.2, the underlined values represent the real pressures at equilibrium; from 1500–2546 K, the silicon partial pressures due to reaction (7.23) are the real ones. The pressures of silicon vapor under these conditions are less than the pressure at saturated conditions, and therefore, in this temperature interval the dissociation takes place in the gas phase. As a result of reactions (7.23) and (7.25), carbon gradually accumulates in the silicon carbide charge.

At temperatures above 2546 K, the partial pressure of silicon due to reaction (7.25) becomes greater than that by reaction (7.23). Therefore, reaction (7.23) cannot take place ($\Delta G_T^0 > 0$) and the pressure of silicon above SiC is regulated only by reaction (7.25). In Table 7.2, the values due to reaction (7.25) are underlined from 2546–2900 K, which represent the real ones. According to Lilov [24], above 2546 K, silicon is separated in the form of the solution saturated with carbon. In this case, the activity of Si in the solution is equal to the equilibrium constant of reaction (7.22), $K_1 = a_{Si}$. The partial pressure of silicon can be obtained according to Henry's law $P_{Si} = P_{Si}^{Sat}\, a_{Si}$ and the partial pressure of $SiC_2$ can be determined from the equation, $P_{SiC_2} = \dfrac{K_4}{K_1 P_{Si}^{sat}}$.

**Table 7.2.** Partial pressures of Si and $SiC_2$ (Pa) (Lilov [24])

| T [K] | $P_{Si}^{Sat}\, a_{Si}$ | $P_{Si}$ reaction (7.23) | $P_{Si}$ reaction (7.25) | $P_{SiC_2}$ reaction (7.25) |
|---|---|---|---|---|
| 1500 | $3.5 \times 10^{-5}$ | $\underline{3.0 \times 10^{-6}}$ | $3.9 \times 10^{-7}$ | $5.1 \times 10^{-8}$ |
| 1600 | $4.4 \times 10^{-4}$ | $\underline{4.2 \times 10^{-5}}$ | $7.6 \times 10^{-6}$ | $1.4 \times 10^{-6}$ |
| 1700 | $4.0 \times 10^{-3}$ | $\underline{4.3 \times 10^{-4}}$ | $1.0 \times 10^{-4}$ | $2.5 \times 10^{-5}$ |
| 1800 | $2.5 \times 10^{-2}$ | $\underline{3.4 \times 10^{-3}}$ | $1.0 \times 10^{-3}$ | $3.2 \times 10^{-4}$ |
| 1900 | 0.11 | $\underline{2.2 \times 10^{-2}}$ | $8.3 \times 10^{-3}$ | $3.2 \times 10^{-3}$ |
| 2000 | 0.47 | $\underline{0.11}$ | $5.3 \times 10^{-2}$ | $2.5 \times 10^{-2}$ |
| 2100 | 1.8 | $\underline{0.52}$ | 0.28 | 0.16 |
| 2200 | 5.8 | $\underline{2.0}$ | 1.3 | 0.84 |
| 2300 | 17 | $\underline{7.0}$ | 5.2 | 3.8 |
| 2400 | 47 | $\underline{22}$ | 18 | 15 |
| 2500 | 116 | $\underline{61}$ | 58 | 56 |
| 2546 | 173 | $\underline{97}$ | 96 | 96 |
| 2600 | 270 | 161 | $\underline{170}$ | 170 |
| 2700 | 588 | 391 | $\underline{456}$ | 456 |
| 2800 | 1210 | 890 | $\underline{1138}$ | 1138 |
| 2900 | $\underline{2366}$ | 1914 | 2659 | 2659 |
| 3000 | $\underline{4419}$ | 3904 | 5855 | 5855 |
| 3100 | $\underline{7922}$ | 7604 | 12250 | 12250 |
| 3150 | $\underline{10477}$ | 10477 | 17418 | 17418 |

At temperatures above 2900 K, the partial pressure of Si determined by the equilibrium constant of reaction (7.25) becomes more than the pressure of silicon saturated vapor and therefore the dissociation of SiC takes place in the condensed phase accompanied by the separation of liquid silicon. In Table 7.2, these values are underlined in the column $P_{Si} = P_{Si}^{Sat}\, a_{Si}$, that are obtained using Henry's law.

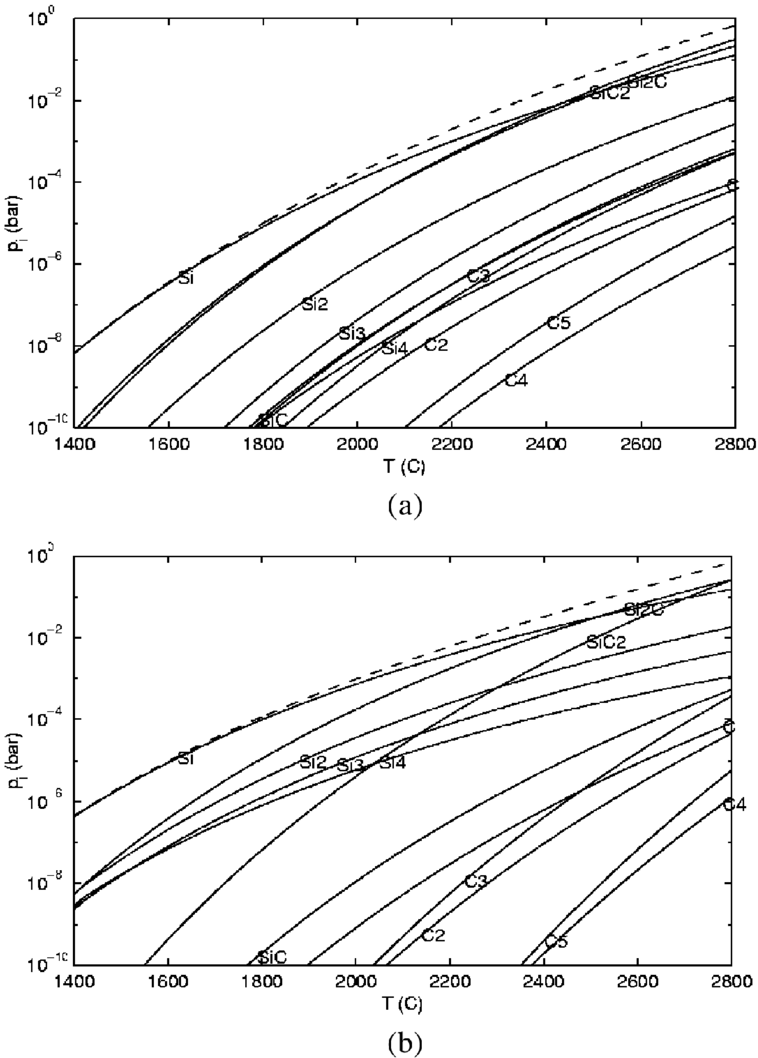


**Fig. 7.4.** Equilibrium partial pressures for various species in a Si-C system assuming (a) condensed SiC and carbon, (b) condensed SiC and silicon. The dashed line is the total pressure [19].

At 3150 K, $K_1 = a_{Si} = 1$ and $P_{SiC_2} = K_4 / P_{Si}^{Sat}$, the solution of C in Si becomes mutually saturated. At T > 3150 K, $\Delta G_T^0$ of reaction (7.22) is less than zero, and therefore, SiC under these conditions dissociates completely. Hence, 3150 K is the limiting temperature for the existence of SiC in the condensed phase.

Figure 7.4(a) shows the equilibrium pressures of a Si-C system at constant pressure. The gaseous species include C, $C_2$, $C_3$, $C_4$, Si, $Si_2$, $Si_3$, SiC, $SiC_2$, and $Si_2C$, and the condensed species are SiC and carbon. Among individual species gaseous silicon dominates at temperatures below 2673 K, while $SiC_2$ and $Si_2C$ have larger partial pressures at higher temperatures. Figure 7.4(b) shows the system with condensed SiC and silicon. Since liquid silicon is energetically less favorable, it only occurs when there is excess of silicon and no carbon source. The partial pressures are higher as shown in Fig. 7.4(b).

### *Growth kinetics*

As explained above, reaction (7.25) is considered most important for the deposition process (Lilov [24]). The vapor pressure of silicon is larger than that of $SiC_2$ at temperatures below 2546 K, and less than that of $SiC_2$ at temperatures above 2900 K. The rate-determining species, A, is therefore chosen as $SiC_2$ at $T < 2546$ K, and as Si at $T > 2900$ K. A can be either of the two at 2546 K $< T <$ 2900 K, since they have the same vapor pressure (Table 7.2). Introducing $z'$ coordinate, which is set as 0 at the charge and $L$ at the seed, vapor pressures of various species can be considered as a function of $z'$.

To develop a growth kinetics model, Chen et al. [11,13] have assumed that the species transport rate near the seed is proportional to supersaturation of A, such that [39],

$$J_A = \chi_A \left(p_A(L) - p_A^*(L)\right), \tag{7.29}$$

where $p_A^*$ is the equilibrium vapor pressure of A, $\chi_A = \frac{1}{\sqrt{2\pi M_A RT}}$. If $SiC_2$ and Si vapors can be assumed to have an identical transport rate, i.e., $J_{SiC_2} = J_{Si}$, the growth rate of SiC crystal will become,

$$G_{SiC} = \frac{2M_{SiC}}{\rho_{SiC}} \chi_A [p_A(L) - p_A^*(L)] \tag{7.30}$$

A multiple 2 is introduced on the right side of Eq. (7.30) since one $SiC_2$ molecule and one Si molecule form 2 SiC molecules.

Assuming that advective velocities of the species $SiC_2$ and Si are the same, the distribution of vapor pressure can be obtained from a one-dimensional mass transfer equation for Stefan flow as,

$$p_{SiC_2}(z') + p_{Si}(z') = p - [p - p_{SiC_2}(0) - p_{Si}(0)] \exp(Pe \cdot z'/L) \tag{7.31}$$

The advective velocity, $U$, in $Pe$ can be expressed as a function of transport rate of $SiC_2$ and Si,

$$U = J_{SiC} RT/p = 2\chi_A (p_A(L) - p_A^*(L)) RT/p \tag{7.32}$$

From the above equation, one can obtain,

$$p_A(L) = p_A^*(L) + Up/(2\chi_A RT) \tag{7.33}$$

If $Si_2C$ and Si can be assumed to have an identical vapor pressure in the growth chamber, equation (7.31) will reduce to,

$$U = D/L \ln((p - 2p_A(L))/(p - 2p_A(0)) \tag{7.34}$$

Even if there exists a difference between the equilibrium vapor pressures of the two species at the charge, the above equation is still valid.

Furthermore, if the vapor pressure at the source is assumed to be the same as the equilibrium vapor pressure, such that $p_A(0) = p_A^*(0)$, $U$ and $p_A(L)$ can be obtained from Eqs. (7.33) and (7.34) by solving them in an iterative fashion. First, by setting $U$ as 0, $p_A(L)$ can be calculated using (7.33), the advective velocity $U$ can then be obtained by substituting (7.33) in (7.34), and finally the growth rate can be calculated using (7.30). Here the equilibrium vapor pressures of species Si, SiC, $Si_2C$, and $SiC_2$ can be taken from (7.24) as partly shown in Table 7.2.

### 7.2.6 Numerical method

The transport equations for electromagnetic field, heat transfer, and species transport can be solved by using a numerical scheme based on either finite element (Pons et al. [4]; Egorov et al. [6]) or finite volume method (Hofmann et al. [2]; Chen et al. [13]). Pons et al. [4] have used an FEM package "Flux-Expert", which alternately solves the electromagnetic and thermal equations without an external iterative scheme. Once the temperature field is obtained, the mass transfer equations are solved in an uncoupled manner. The computer model developed by Hofmann et al. [2] uses the basic finite volume code FASTEST (developed at the University of Erlangen) that also employs multigrid techniques.

Chen and co-workers [13], on the other hand, have developed their computer model for SiC growth using MASTRAPP (Multizone Adaptive Scheme for Transport and Phase Change Processes). MASTRAPP employs high-resolution schemes for grid refinement and clustering for phase-change and moving boundary problems and has been extensively used for crystal growth modeling by Zhang et al. [40,41] and many others. MASTRAPP-based crystal growth simulations have been well tested against the experimental data, and the model is being used for a variety of industrial problems.

The integrated radiative heat transfer equations using the DEF method require special treatment. The coupling between the solvers of energy Eq. (7.13) and radiation Eq. (7.21) is obtained through nodal temperatures and heat fluxes in an iterative fashion. Refer to Chen et al. [13] and Naraghi et al. [34,35] for details on the solution scheme.

A suitable grid distribution with finer mesh in the regions of large temperature and species gradients needs to be used for accurate predictions. For example, Chen

et al. [13] have used a grid of 198 × 147 for most of their calculations (Fig. 7.5). Other investigators have also used very fine grids to perform the growth simulation [2,4,6]. Furthermore, since the electrical and thermal conductivities of the graphite susceptor strongly depend on the temperature (Table 7.3), the heat power generated in the graphite susceptor changes significantly with time. It is therefore necessary to use a small time step, e.g., 2 s for the transient calculations.

A typical solution procedure is adopted as follows: The electromagnetic field (Eq. 7.10) is solved to obtain the heat generated by induction heating (Eq. 7.12), which is added as a heat source term in the energy equation (Eq. 7.13) to obtain the temperature distribution solved together with Eq. (7.21). After obtaining the temperature field, mass transfer, and vapor species concentration, growth rate can be obtained using a one-dimensional mass transfer model coupled with a growth kinetics model (Section 7.2.5). The radial variation of growth rate is considered by taking into account the temperature variation in the radial direction. The model can therefore predict two-dimensional growth interface profile except that mass transfer and thermal coupling are not allowed in the lateral direction.

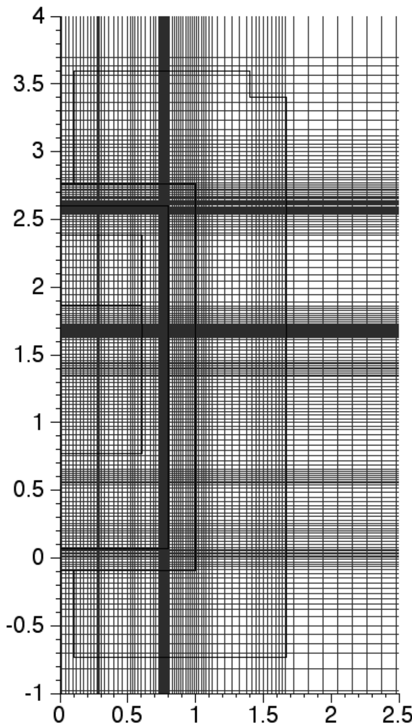


**Fig. 7.5.** Computational grids for finite volume method [13]. Grids are highly clustered in the regions of large temperature gradients.

**Table 7.3.** Material properties of various components [13]

| Components | Electrical resistivity [Ωm] [500–3000°C] | Thermal conductivity [W/m/K] [500–3000°C] |
|---|---|---|
| Graphite | $0.8 \times 10^{-5}$–$1 \times 10^{-5}$ | 50–20 |
| Insulation | 0.001 | 0.1–3 |
| SiC crystal | 1–0.001 | 100–50 |
| SiC charge | 1–0.001 | 20–5 |
| Argon | — | 0.03–0.05 |

## 7.3 Growth Simulation

### 7.3.1 Electromagnetic field and heat generation

In calculating the electromagnetic field, it is necessary to consider reasonable axial and radial distances in the computational domain such that most of the contours of magnetic potential vector, $A$, remain within the field of simulation. This is important for application of the boundary condition [11] and accurate calculation of the heat generated in the graphite susceptor. For example, Chen et al. [13] have taken the computational domain as $-20R_s < z < 20R_s$ and $r < 20R_s$ with the radius of the outer surface of the susceptor $R_s = 70$ mm for a 75 mm diameter crystal growth. In this case, the magnetic potential is diminished at a distance of $20R_s$ from the coil. Many times, it is necessary to perform calculations with different sizes of the computational domains to make an appropriate choice. Typical contours of magnetic vector potential for 5 turns of coil and current of 1200 $A$ as obtained by Chen et al. [11] are shown in Fig. 7.6. The contour lines are concentrated along the outer portion of the graphite susceptor, and the contour of $(A_0)_{real} = 5 \times 10^{-5}\ Wb/m$ bends in the bottom and top portion of the susceptor and passes through the outer portion of the cylindrical susceptor. The graphite susceptor with a high conductivity serves as a shield, such that a large amount of energy is generated by eddy currents in the susceptor within a small skin depth, leaving less energy to be generated in the parts inside the susceptor (like the crucible, crystal, and charge).

The generated heat per unit volume for the case considered by Chen et al. [13] is shown in Fig. 7.7. Clearly, $q'''_{eddy}$ in the susceptor is several orders of magnitude larger than that in the SiC charge. The total amount of energy generated in the skin depth is much larger because of the volume for the same radial width becomes larger (second power) away from the central axis.

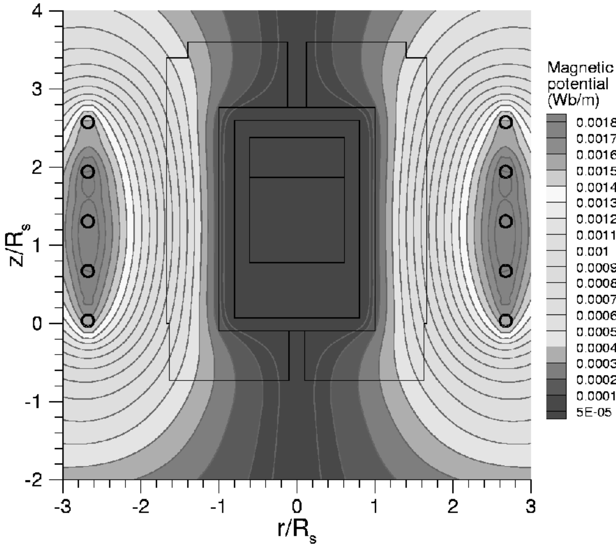


**Fig. 7.6.** magnetic potential contours, $(A_0)_{real}$, in a system with a coil of five turns, current of 1200 A and frequency of 10 kHz [13]. Only a portion of the computational domain, $r \leq 3R_s$ and $z \leq 4R_s$, is shown in this figure.

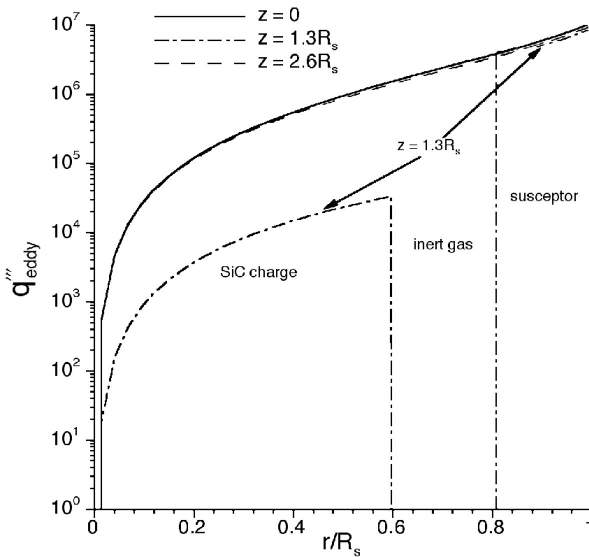


**Fig. 7.7.** Generated heat power, $q'''_{eddy}$, along the radial direction at different heights $z = 0$, $1.3R_s$, and $2.6R_s$. The profile at $z = 1.3R_s$ has an inert gas gap between the powder charge and the susceptor [13].

### 7.3.2 Temperature field

Axial and radial temperature gradients are crucial for the successful growth and enlargement of SiC crystals. The SiC charge sublimes in the bottom of the container where the temperatures are higher than that in the seed, and saturation of the SiC vapor is thus produced in the SiC charge region. Since temperature on the seed surface is lower than that in the powder charge, the SiC vapor becomes supersaturated near the seed. The supersaturation of vapor species acts as a driving force for the deposition of SiC. The growth rate is therefore not only related to the temperature at the seed but also to the axial temperature gradient. Balkas et al. [42] have found that for a given seed temperature, the growth rate is a linear function of the temperature gradient in the growth chamber.

A positive radial temperature gradient at the seed surface can initiate an outward growth especially when a Lely seed is used to grow large size crystals, and depress the polytype growth on the graphite lid near the seed. The lower temperature at the center of the seed can ensure a higher growth rate on the seed than that on the graphite lid, because the supersaturation of the vapor species is higher on the seed.

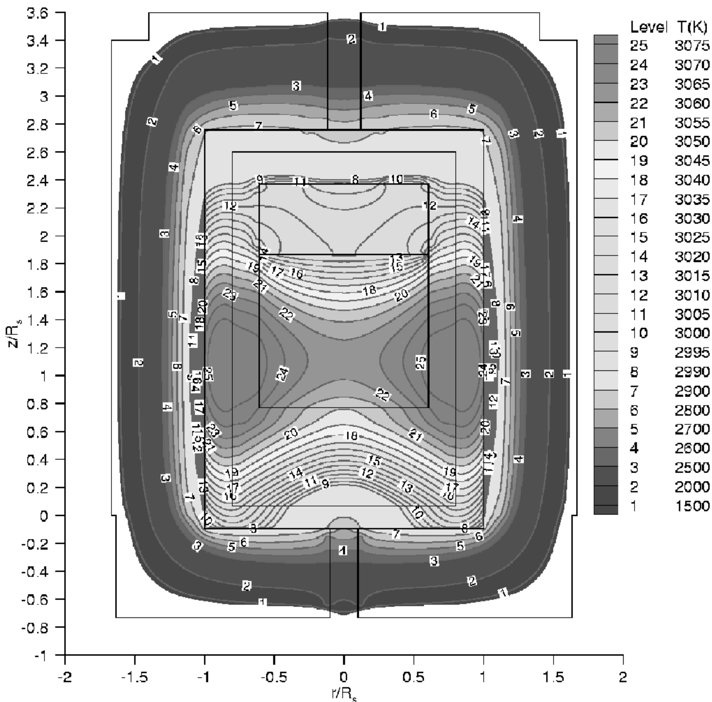


**Fig. 7.8.** Temperature contours for a system with a coil of five turns, current of 1200A, frequency of 10 kHz, and inert gas pressure of 26,666 Pa [11]

As shown by Chen and other investigators (Fig. 7.8), the maximum temperature exists in the graphite susceptor and always at the level of the geometric center of the induction coil. The positive temperature difference between the SiC charge and the seed allows the sublimation of SiC in the charge and deposition of SiC on the seed. A positive radial temperature gradient is also formed at the seed surface, which ensures an outward growth of the crystal [43]. As can be seen in Fig. 7.8, the temperature difference is less than 10 K at the seed surface. A proper radial temperature gradient at the seed has to be obtained to ensure a convex shape of the crystal interface and keep thermal stresses low in the crystal as well as low dislocation and micropipe densities.

### *Temperature distribution for different currents*

The temperature distribution strongly depends on the power supply to the RF coil (see Fig. 7.9 for $I$ = 1000 A and 1100 A and Fig. 7.8 for $I$ = 1200 A). The magnitude of the temperature increases with the current. The growth temperature for the modified Lely method ranges from 1800 K to 2900 K as reported by Tairov and Tsvetkov [44,45]. The temperature distribution for the case of $I$ = 1200 A corresponds to an upper limit growth condition for the modified Lely method in the system considered by Chen et al. [11]. The growth temperature depends on the temperature gradient that is related to the system design. For systems with a large temperature gradient, the growth temperatures are low (2100–2800 K) (Tairov and Tsvetkov [44,45]; Barrett et al. [22,23]; Hofmann et al. [2,3]; Müller et al. [7]),

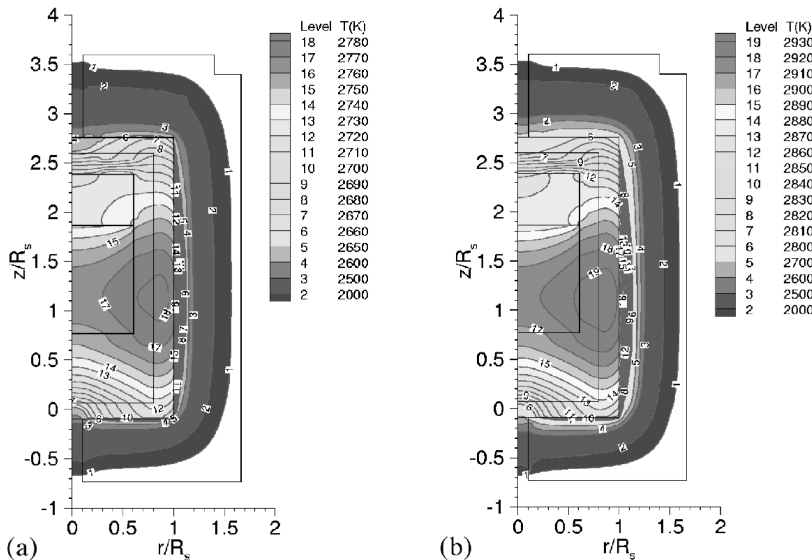


**Fig. 7.9.** Temperature distributions for different currents, (a) $I$ = 1000 A, and (b) $I$ = 1100 A [13]

while the growth temperatures range from 2700 K to 2900 K for systems that have smaller temperature gradients (Pons et al. [4,5]). For a low growth temperature, the inert gas pressure required is lower than that required for the high temperature growth.

As can be seen in Figs. 7.8 and 7.9, the temperature has a lower value at the center of the seed because of the cooling effect of the upper hole. The temperature increases along the radial direction on the seed surface, reaches a high value before the inner wall of the growth chamber. The lower temperature at the center of the seed can ensure an outward growth in radial direction, because of higher supersaturation of the vapor species at the center of the seed than that near the edge of the seed. Management of heat loss is crucial to control the growth of SiC crystals. However, it is not an easy task since thermal characteristics of the upper portion of the crucible change significantly as the growth proceeds and thermal resistance due to as-grown crystal increases. This task is made further difficult because currently the heat loss system used for PVT growth is passive.

### *Temperature for different coil positions*

As is well known, by moving the induction coil upward/downward, the temperature difference between the charge and the seed can be easily changed. Figure 7.10 presents the temperature distributions for two different positions ($z_{coil}$ = 0, 10 mm), while the temperature on the top of the crucible is kept at 2400 K. A PID (propor-

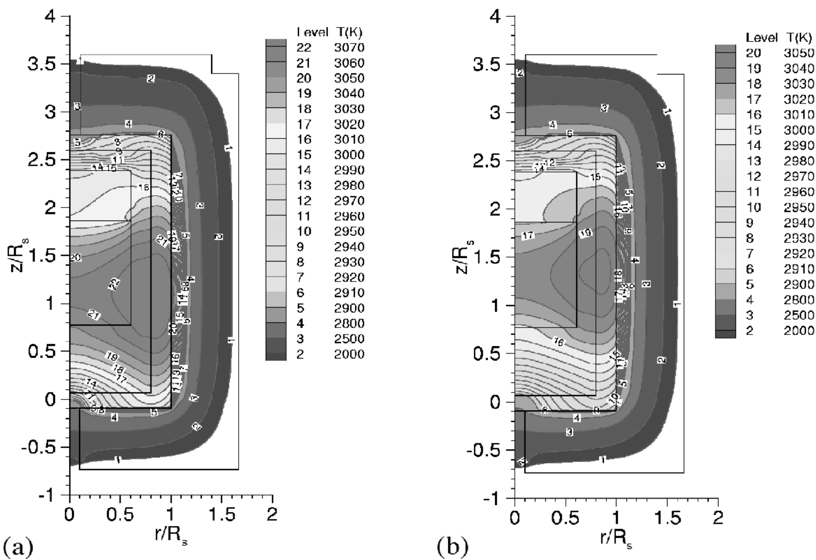


**Fig. 7.10.** Temperature distributions for different coil positions. The coil positions are (a) $z_{coil}$ = 0 and (b) 0.01 m, respectively. The temperature on top of the crucible is kept at 2400 K for all the cases [13].

tional, integral, and derivative) control strategy has been used numerically to keep the temperature on top of the crucible constant by changing the current. With the coil moved up, the location of the maximum temperature in the charge moves up and the temperature difference between the charge and the seed decreases. In Figs. 7.10(a–b), the temperature difference between the charge and the seed, $T_{charge} - T_{seed}$, is a linear function of the coil position, $z_{coil}$. It should be noted that the temperature difference may not remain a linear function of the coil position if the coil is moved further up. Since the growth rate depends on the temperature difference between the charge and the seed (Eq. 7.35), the change in coil position will certainly affect the growth rate.

### *Temperature distribution for different ingot length*

The temperature distribution also changes with the growth of crystal (Fig. 7.11). A large radial temperature gradient during the initial growth is important for enlargement of the crystal. After the ingot length of the crystal reaches 5 mm for the system considered here, the radial temperature gradient decreases (Figs. 7.11a–b). A small radial temperature gradient ensures a constant diameter of the crystal and relatively flat growth interface. More importantly, the thermal stress in as-grown crystal caused by temperature gradient decreases after the ingot length exceeds 5 mm. The axial temperature gradient in the ingot crystal is about 15 K/cm after the ingot of 25 mm has been grown (Figs. 7.11a–b).

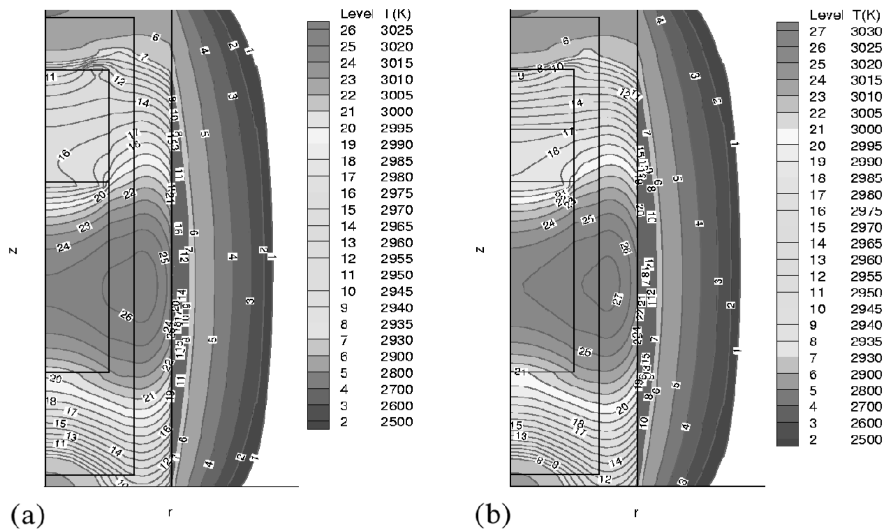


**Fig. 7.11.** Temperature distributions in a 35mm system when I = 1350 A, and ingot length (a) $L_{in} = 0$ and (b) $L_{in} = 25$ mm

Simulations reported by various investigators demonstrate that the temperature and temperature gradient inside the crucible are strong functions of system design, coil position, power supply, charge size, and ingot length. In addition, the temperature field continuously changes with an increase in the crystal length. The simulations reported in literature thus far give a good qualitative understanding of the effect of these parameters. However, simulations need to be performed every time a change in the design of the system is contemplated.

### 7.3.3 Growth rate calculations

The experimental data of Balkas et al. [42] indicate that the growth rate is a linear function of the temperature difference between the seed and source, $\Delta T$, and an exponential function of the inverse of growth temperature with the following expression,

$$G_{SiC} = A\,(p, S, t)\,\Delta T \exp(-U/RT), \tag{7.35}$$

where $U$ is the activation energy, $A\,(p, S, t)$ is a coefficient that depends on the inert gas pressure $p$, the effective source surface area $S$, and the duration of the growth, $t$. Balkas et al. [42] found that $U = 5.99 \times 10^5$ J/mol based on their experiment data.

#### *Dependence of growth rate on growth temperature*

Chen et al. [11] have investigated the dependence of growth rate on growth temperature for a range of axial temperature gradients. They have considered two cases, one with a small axial temperature gradient of 2 K/cm, and the other with a large axial temperature gradient of 20 K/cm. The distance between the seed and the charge surface is taken as 5 cm (2 inch).

The growth rate predicted by Chen et al. [11] shows an Arrhenius-type dependence on the growth temperature for inert gas pressures ranging from 666 Pa (5 Torr) to 40,000 Pa (300 Torr) (Fig. 7.12). The growth rate curves, however, deviate from the Arrhenius behavior when the temperature becomes too high. The Arrhenius-type growth curve for a given pressure shifts towards the low temperature region when the axial temperature gradient increases (compare Fig. 7.12b with 7.12a). The low temperature growth, that is usually associated with small-scale systems, therefore, requires a larger axial temperature gradient (Fig. 7.12b). The experimental data for 700 Pa argon pressure in Fig. 7.12b taken from Nakata et al. [46] support the prediction of Chen et al. [11] at low pressures.

In the growth rate–growth temperature map, the curves merge at high temperatures where the total vapor pressure of species is larger than the inert gas pressure (Fig. 7.12). In this case, if the crucible is not properly sealed, the pressure inside the crucible will fluctuate since the pressure inside the crucible will be higher than the system pressure. The fluctuation of pressure inside the crucible can cause unsteady species transport in the growth chamber by Stefan flow and growth fluctuations.

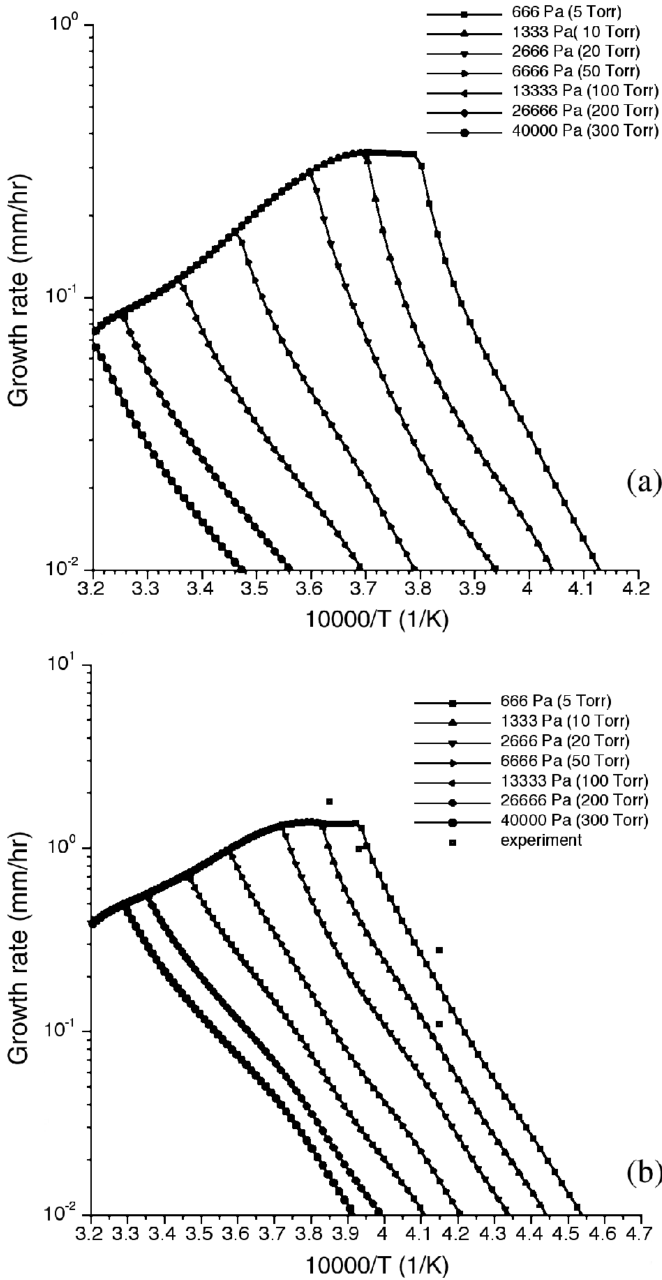


**Fig. 7.12.** Predicted growth rate versus inverse of growth temperature for different gas pressures for axial temperature gradients of (a) 2 K/cm and (b) 20 K/cm [11]. Experimental data for inert gas pressure of 700 Pa in (b) are taken from Nakata et al. [46]

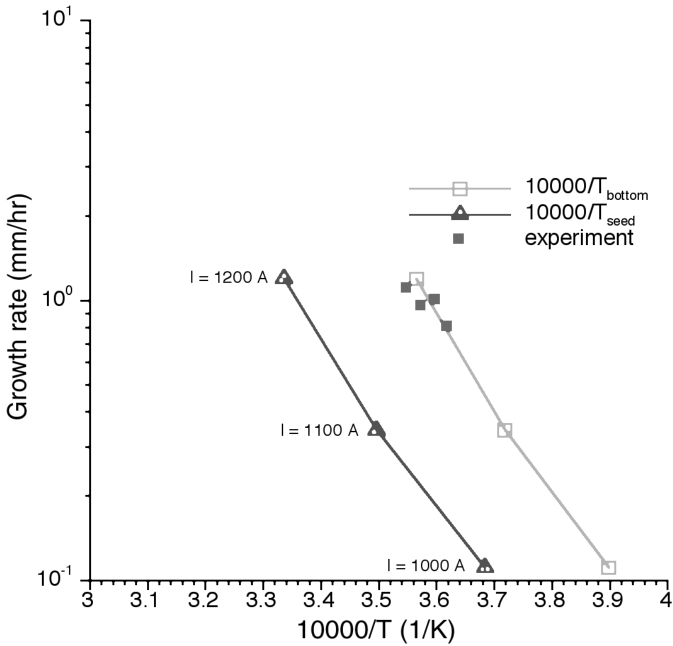


**Fig. 7.13.** Dependence of the growth rate on the seed temperature, $T_{seed}$, and the temperature on the bottom of the crucible, $T_{bottom}$ in a 75 mm system [15]. The symbols from top to bottom correspond to currents of 1200 A, 1100 A, and 1000 A, respectively. Experimental data are taken from Balkas et al. [42]

The growth rate versus growth temperature curve in Fig. 7.13 is an Arrhenius-type curve and yields an activation energy of $5.5 \times 10^5$ J/mol, close to $5.44 \times 10^5$ J/mol as reported by Syväjärvi et al. [47]. The growth rate versus the inverse of the temperature at the bottom is also plotted in Fig. 7.13 and yields the same activation energy as the previous curve. The predicted growth rate at high pressures strongly depends on the diffusion coefficient $D_0$, which is in the range of $5 \times 10^{-6} \sim 2 \times 10^{-4}$, taken as $1 \times 10^{-5}$ $m^2/s$ by Chen et al. [13] to better correlate the prediction with experimental data of Balkas et al. [42].

#### *Influence of inert gas pressure on growth rate*

Chen et al. [11] have also examined the dependence of growth rate on inert gas pressure for the previous two cases. The growth rate curves become flat when the inert gas pressure is low. Although the growth rate of about 1 mm/h cannot be achieved for an axial temperature gradient of 2 K/cm (Fig. 7.12a), it is possible to obtain such a growth if the axial temperature gradient of 20 K/cm can be maintained at $T_{seed} > 2400$ K (Fig. 7.12b). From Fig. 7.14, it is evident that it is theoretically

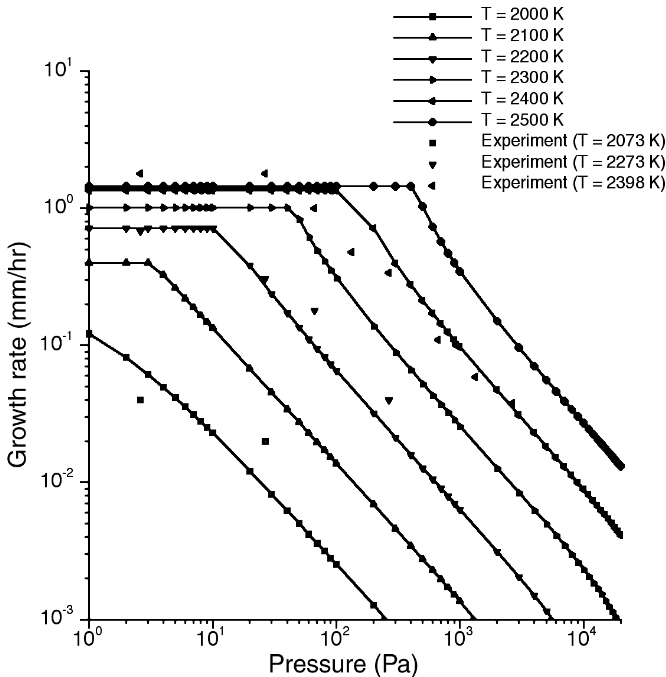


**Fig. 7.14.** Growth rate versus gas pressure for different growth temperatures at axial temperature gradient of 20 K/cm [11]

possible to grow SiC crystals at elevated inert gas pressures, such as 26,666 Pa (200 Torr), if the growth temperature is high. On the other hand, the growth at pressures less than 133 Pa (1 Torr) and temperatures below 2500 K is also possible, as shown in Fig. 7.14.

Figure 7.14 also shows that when the inert gas pressure is low, the growth rate does not increase as the pressure is decreased. This is because the total vapor pressure of SiC species is larger than the inert gas pressure. The growth is therefore unstable in this case, and a leak in the crucible will cause fluctuations in the pressure inside the crucible and unsteady growth conditions.

## *Dependence of growth rate on temperature gradient*

As is well known, the temperature gradient in the substrate region is an important parameter for CVD growth, but in the PVT growth of SiC crystals, the effect of this parameter has not been examined carefully. Chen et al. [11] have made the first attempt to study the importance of temperature gradient as presented in Fig. 7.15 where the growth rate versus inert gas pressure is presented for several different temperature gradients, for the growth temperature of 2400 K. With an increase

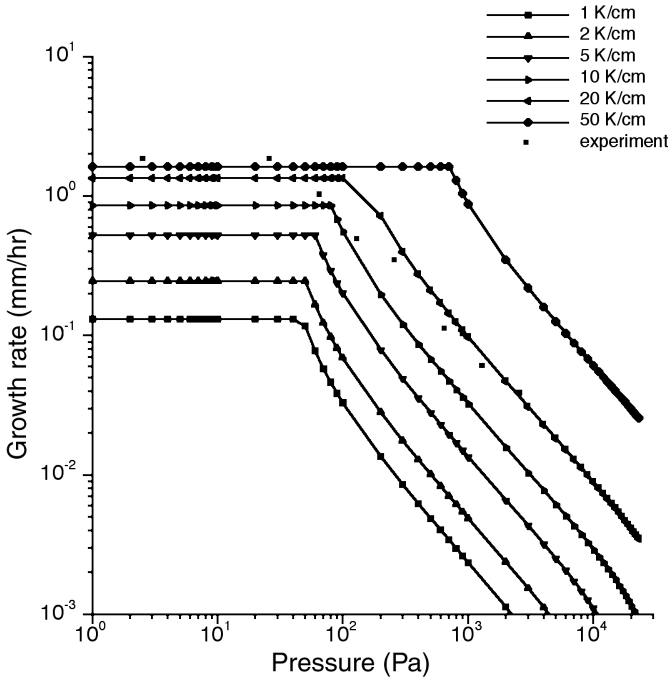


**Fig. 7.15.** Growth rate versus gas pressure for different axial temperature gradients at growth temperatures of 2400 K [11]. Experimental data are taken from [17]

in temperature gradient, the growth rate curve moves upward towards the high growth rate region. Again, in the growth rate–inert gas pressure map, the region where the growth rate curves become flat will have unstable growth, since the total vapor pressure of SiC species will be higher than the inert gas pressure.

### *Effect of coil position on temperature distribution and growth rate profile*

Since $T_{charge} - T_{seed}$ is related to the coil position, the growth rate can be changed by moving the coil upward or downward. There are different control strategies, such as keeping the temperature on the top of the crucible, $T_{top}$, constant (Chen et al. [13]), or by keeping the power supply constant (Selder et al. [16]). The growth rate versus temperature difference between the charge and the seed is shown in Fig. 7.16 for different coil positions when $T_{top}$ is kept constant, at 2400 K or 2300 K. In a certain range of coil position, the growth rate is a linear function of coil position, $z_{coil}$. For example, for $T_{top}$ = 2400 K, the growth rate is almost a linear function of $z_{coil}$ when $0 < z_{coil} < 0.03$ m; and for $T_{top}$ = 2300 K, the growth rate is a linear function for $-0.03 \text{ m} < z_{coil} < 0$. The growth rate can be less than zero representing etching of the seed (not shown here), if the coil is moved further up.

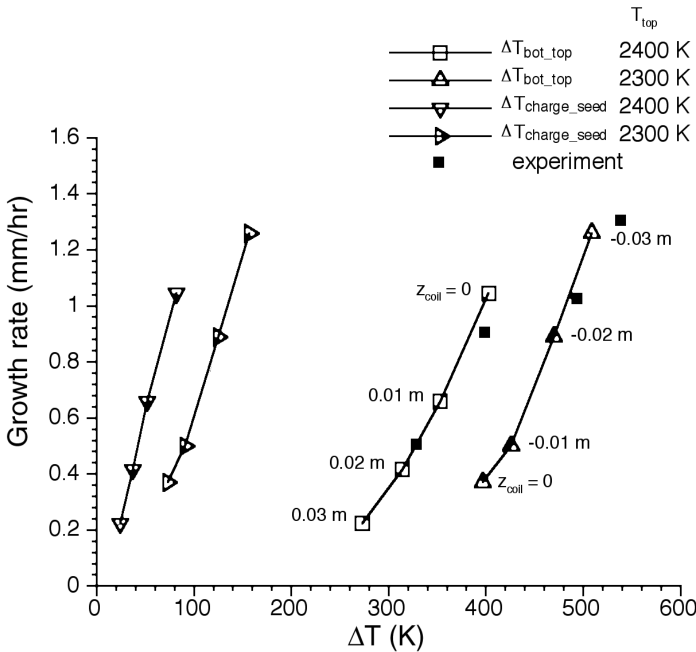


**Fig. 7.16.** Dependence of growth rate, $G_{SiC}$, on temperature difference between the charge and seed, $T_{charge} - T_{seed}$, and on temperature difference between the bottom and top of the crucible, $T_{bottom} - T_{top}$. The coil positions, $z_{coil}$, are denoted besides the symbols on the curve of $G_{SiC} \sim T_{bottom} - T_{top}$. The temperature on the top of the crucible, $T_{top}$, is maintained at either 2400 K or 2300 K [13]. Experimental data are taken from Balkas et al. [42]

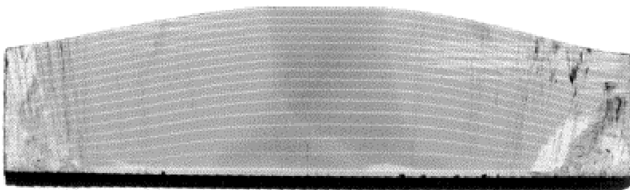

**Fig. 7.17.** Slice of a SiC crystal marked during growth by interface demarcation technique. The seed is positioned at the bottom. Dark horizontal regions are nitrogen-rich SiC material, undoped regions exhibit a bright contrast (Selder et al. [16])

The effect of coil position has also been studied by Selder et al. [16] who used an interface demarcation technique to achieve the experimental surface shape. During the growth experiment, nitrogen was added to the inert gas in the growth cell at fixed time steps. After the growth experiment, a slice was cut from the grown crystal along its growth direction as shown in Fig. 7.17.

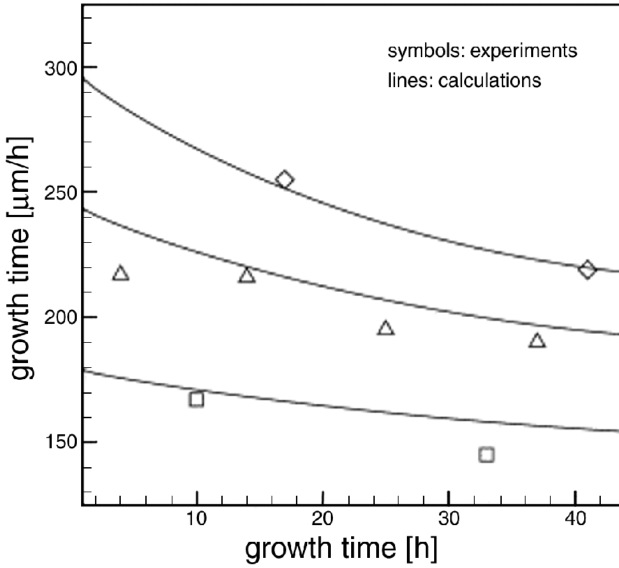


**Fig. 7.18.** Measured and predicted growth rates for different coil positions. Starting from a symmetrical coil position (upper curve), the coil is successively shifted downwards (Selder et al. [16])

Growth rate evolution in the center of the crystal was measured and computed for different coil positions while keeping the induction power constant. Figure 7.18 shows that the growth rate decreases with increasing crystal length. As can be seen, the growth rate also decreases by shifting the coil downward while the power supply is held constant. This is because the growth temperature, $T_{seed}$, decreases although $T_{charge} - T_{seed}$ may increase.

### 7.3.4 Thermally induced stress

Thermal stresses in SiC crystal with nonuniform temperature gradient can cause plastic deformation and generation of dislocations during the growth. Müller et al. [8] have used a thermoelastic model to calculate the thermal stress based on the temperature field from their 2D model. The stress-strain relation for a thermoelastic anisotropic solid body is taken as [48,49]:

$$\begin{pmatrix} \sigma_{rr} \\ \sigma_{\varphi\varphi} \\ \sigma_{zz} \\ \sigma_{rz} \end{pmatrix} = \begin{pmatrix} c_{11} & c_{12} & c_{13} & 0 \\ c_{12} & c_{22} & c_{23} & 0 \\ c_{13} & c_{23} & c_{33} & 0 \\ 0 & 0 & 0 & c_{44} \end{pmatrix} \begin{pmatrix} \varepsilon_{rr} - \alpha(T - T_{ref}) \\ \varepsilon_{\varphi\varphi} - \alpha(T - T_{ref}) \\ \varepsilon_{zz} - \alpha(T - T_{ref}) \\ \varepsilon_{rz} \end{pmatrix} \tag{7.36}$$

In the above equation, α is the thermal expansion coefficient, $T_{ref} = 0.5(T_{\min} + T_{\max})$ is a reference temperature, and

$$\varepsilon_{zz} = \frac{\partial u}{\partial z}, \qquad \varepsilon_{rr} = \frac{\partial u}{\partial r}, \qquad \varepsilon_{\varphi\varphi} = \frac{v}{r}, \qquad \varepsilon_{rz} = \frac{\partial v}{\partial z} + \frac{\partial u}{\partial r}, \tag{7.37}$$

$c_{ij}$ are the elastic material constants in the Voigt notation and $u$, $v$ are the displacement components in axial and radial direction, respectively. Figure 7.19 shows the calculated 2D temperature distribution and the corresponding 2D distribution of the normal component $\varepsilon_{rr}$, and shear stress $\varepsilon_{rz}$ in the crystal area, with positive values corresponding to tension and negative values to compression [8]. The calculated level of thermoelastic stress up to ~ 100 MPa in the SiC crystal during growth is well above the critical resolved shear stress $\sigma_{CRS}$, ~ 8 MPa (4H-SiC) and ~ 13 MPa (6H-SiC) at 1300°C (Samant and Pirouz [50]). The resolved shear stress at 2200–2500°C is < 1 MPa by extrapolating the experimental values according to Müller et al. [8]. The generated dislocations are estimated to be N $\propto$ $(|\sigma_{RS}| - \sigma_{CRS})$.

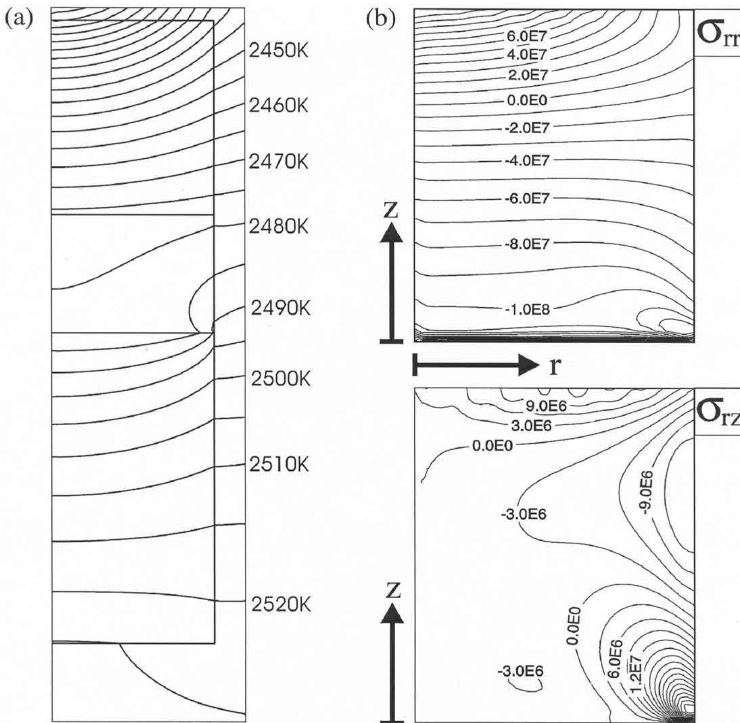


**Fig. 7.19.** (a) Numerical simulation of the axisymmetric temperature distribution inside a growth cell, and (b) resulting thermoelastic stress inside a 6H-SiC crystal: normal stress, $\sigma_{rr}$, and shear stress, $\sigma_{rz}$ (Müller et al. [8])

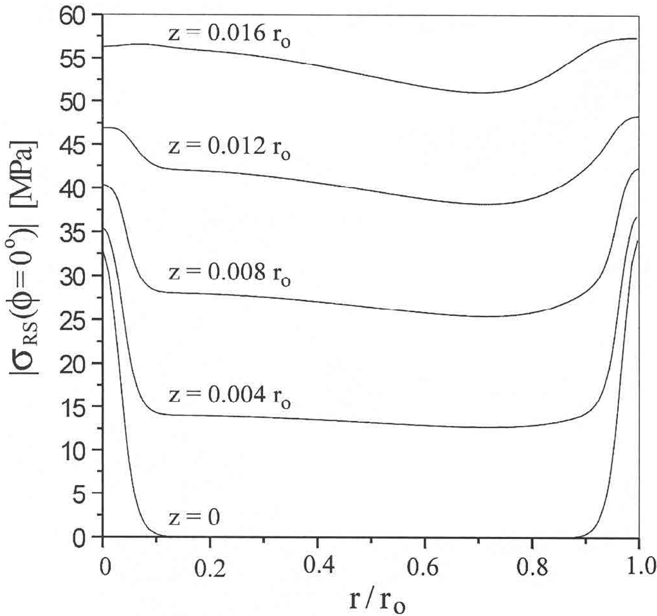


**Fig. 7.20.** Radial dependence of the resolved shear stress in the < $11\bar{2}0$ > direction at different distances from the growth interface ($z = 0$) (Müller et al. [8])

For the three primary (0001) < $11\bar{2}0$ > slip systems $\sigma_{RS}$ is given by $\sigma_{RS} = (\sigma_{rr} + \sigma_{rz})\cos\phi - \sigma_{\phi\phi}\sin\phi$. Figure 7.20 shows the radial dependence of $|\sigma_{RS}|$ for $\phi = 0^\circ$, corresponding to the < 1120 > direction, for different $z$-positions within a thin boundary layer (~ 500 μm) at the growth interface.

Modeling of stresses during the growth of SiC crystals is quite challenging and not much has been reported on this problem except the work of Müller et al. [8]. It is expected that this topic will receive significant attention in the near future because of the direct relationship between the stresses and defects.

## 7.4 Summary

The vapor transport growth of silicon carbide crystals involves induction heating, electromagnetic field, radiative and conductive heat transfer, sublimation and condensation, chemical reaction, stoichiometry, mass transport, thermal stresses, as well as defect and micropipe generation and propagation. The irregular geometry, complicated boundary conditions, and lack of information on thermophysical properties at high temperatures make this process very difficult to understand, model, and control. Since defects and micropipes in SiC crystals are directly related to transport phenomena, it is critical to develop better understanding of these

phenomena to grow crystals of higher quality and larger size and to examine the effects of various parameters individually and collectively.

Models of sufficient complexity have been developed to simulate the sublimation SiC growth [2–19]. These models account for the RF heating, heat generation in graphite susceptor by eddy currents, heat transfer by conduction and radiation, species transport, growth kinetics, and stress analysis. The predictions made by these models are generally in good agreement with experimental data. The growth kinetics and mass transport from the charge to seed determine the growth rate and the shape of the crystal. The growth rate is a strong function of the interface temperature, temperature gradient, inert gas pressure, and the gap between the charge and seed, as well as the charge properties (particle size, height).

Modeling and simulation has been widely used in industry to optimize the system geometry and growth processes. The components of the growth system can be redesigned in order to grow crystals with low thermal stresses. Industry has used the model to design the furnace for growing 50–100 mm diameter SiC crystals. It is observed that a convex shape of interface can ensure an outward growth to expand a small size seed into a large diameter crystal. However, it can generate large thermal stresses and cause higher defect density. The mechanism of defects and screw dislocations is still not well understood and requires a strong coupling among modeling, growth, and characterization. Only then can a direct correlation among the process conditions, transport phenomena, chemistry, growth behavior, stresses, and defects be developed.

### Acknowledgments

Acknowledgements are due to Sterling Semiconductor, Inc. and Advanced Technology Materials, Inc. for supporting this work though grants from BMDO/IST (managed by ONR, N00014-98-C-0176) and from Defense Advanced Research Projects Agency (F33615-98-C-5412), respectively, to NSF (CTS9876198), to AFOSR and DARPA for a MURI grant (F496209510407), and to ONR (grants N0001140010348 and N000140110302, contract monitor Dr. Colin Wood). Special thanks are also due to C. Balkas and N.K. Yushin of Sterling Semiconductor for helpful discussions and to M. Jacobs of AFOSR for encouragement and support of research on modeling in crystal growth.

## References

1. Dhanaraj G, Huang XR, Dudley M, Prasad V, Ma R-H (2002) Silicon Carbide Crystals — Part I: Growth and Characterization. In: Byrappa K, Ohachi T (eds) Crystal Growth for Modern Technology. William Andrew Publishing, Norwich, NY
2. Hofmann D, Heinze M, Winnacker A, Durst F, Kadinski L, Kaufmann P, Makarov Y, Schäfer M (1995) On the Sublimation Growth of SiC Bulk Crystals: Development of a Numerical Process Model. J Crystal Growth 146:214–219

3. Hofmann D, Eckstein R, Kölbl M, Makarov Y, Müller StG, Schmitt E, Winnacker A, Rupp R, Stein R, Völkl J (1997) SiC-Bulk Growth by Physical-Vapor Transport and its Global Modeling. J Crystal Growth 174:669–674
4. Pons M, Blanquet E, Dedulle JM, Garcon I, Madar R, Bernard C (1996) Thermodynamic Heat Transfer and Mass Transport Modeling of the Sublimation Growth of Silicon Carbide Crystals. J Electrochem Soc 143(11):3727–3735
5. Pons M, Blanquet E, Dedulle JM, Madar R, Bernard C (1997) Different Macroscopic Approaches to the Modeling of the Sublimation Growth of SiC Single Crystals. Mater Sci and Eng B 46:308–312
6. Egorov YuE, Galyukov AO, Gurevich SG, Makarov YuN, Mokhov EN, Ramm MG, Ramm MS, Roenkov AD, Segal AS, Vodakov YuA, Vorob'ev AN, Zhmakin AI (1998) Modeling Analysis of Temperature Field and Species Transport Inside the System for Sublimation Growth of SiC in Tantalum Container. Materials Science Forum 264–268:61–64
7. Müller StG, Eckstein R, Hofmann D, Kadinski L, Kaufmann P, Kölbl M, Schmitt E (1998) Modeling of the PVT-SiC Bulk Growth Process Taking into Account Global Heat Transfer, Mass Transport and Heat of Crystallization and Results on its Experimental Verification. Materials Science Forum 264–268:57–60
8. Müller StG, Glass RC, Hobgood HM, Tsvetkov VF, Brady M, Henshall D, Jenny JR, Malta D, Carter Jr CH (2000) The Status of SiC Bulk Growth From an Industrial Point of View. J Crystal Growth 211:325–332
9. Karpov SYu, Kulik AV, Zhmakin IA, Makarov YuN, Mokhov EN, Ramm MG, Ramm MS, Roenkov AD, Vodakov YuA (2000) Analysis of Sublimation Growth of Bulk SiC Crystals in Tantalum Container. J Crystal Growth 211:347–351
10. Ma R-H, Chen Q-S, Zhang H, Prasad V, Balkas CM, Yushin NK (2000) Modeling of Silicon Carbide Crystal Growth by Physical Vapor Transport Method. J Crystal Growth 211:352–359
11. Chen Q-S, Zhang H, Prasad V, Balkas CM, Yushin NK, Wang S (2001) Kinetics and Modeling of Sublimation Growth of Silicon Carbide Bulk Crystals. J Crystal Growth 224:10–110
12. Chen Q-S, Zhang H, Ma R-H, Prasad V, Balkas CM, Yushin NK (2001) Modeling of Transport Processes and Kinetics of Silicon Carbide Bulk Growth. J Crystal Growth 225:299–306
13. Chen Q-S, Zhang H, Prasad V, Balkas CM, Yushin NK (2001) Modeling of Heat Transfer and Kinetics of Physical Vapor Transport Growth of Silicon Carbide Crystals. J Heat Transfer 123:1098–1109
14. Chen Q-S, Zhang H, Prasad V (2001) Heat Transfer and Kinetics of Bulk Growth of Silicon Carbide. J Crystal Growth 230:239–246
15. Prasad V, Chen Q-S, Zhang H (2001) A Process Model for Silicon Carbide Growth by Physical Vapor Transport. J Crystal Growth 229:510–515
16. Selder M, Kadinski L, Makarov Yu, Durst F, Wellmann P, Straubinger T, Hofmann D, Darpov S, Ramm M (2000) Global Numerical Simulation of Heat and Mass Transfer for SiC Bulk Crystal Growth by PVT. J Crystal Growth 211:333–338
17. Räback P, Nieminen R, Yakimova R, Tuominen M, Janzén E (1998) A Coupled Finite Element Model for the Sublimation Growth of SiC. Materials Science Forum 264–268:65–68

18. Räback P, Yakimova R, Syväjärvi M, Nieminen R, Janzén E (1999) A Practical Model for Estimating the Growth Rate in Sublimation Growth of SiC. Mater Sci and Eng B 61–62:89–92
19. Räback P (1999) Modeling of the Sublimation Growth of Silicon Carbide Crystals. Doctoral dissertation, Helsinki University of Technology, Espoo, Finland
20. Augustine G, Hobgood HMcD, Balakrishna V, Dunne G, Hopkins RH (1997) Physical Vapor Transport Growth and Properties of SiC Monocrystals of 4H Polytype. Phys Stat Sol (b) 202:137–148
21. Siergiej RR, Clarke RC, Sriram S, Agarwal AK, Bojko RJ, Morse AW, Balakrishna V, MacMillan MF, Burk Jr AA, Brandt CD (1999) Advances in SiC Materials and Devices: An Industrial Point of View. Mater Sci and Eng B 61–62:9–17
22. Barrett DL, Seidensticker RG, Gaida W, Hopkins RH, Choyke WJ (1991) SiC Boule Growth by Sublimation Vapor Transport. J Crystal Growth 109:17–23
23. Barrett DL, McHugh JP, Hobgood HM, Hopkins RH, McMullin PG, Clarke RC (1993) Growth of Large SiC Single Crystals. J Crystal Growth 128:358–362
24. Lilov SK (1993) Study of the Equilibrium Processes in the Gas Phase During Silicon Carbide Sublimation. Mater Sci and Eng B 21:65–69
25. Prasad V (1991) Convective Flow Interaction and Heat Transfer Between Fluid and Porous Layers. In: S Kakaç et al (eds) Convective Heat and Mass Transfer in Porous Media. Kluwer, Netherlands 563–615
26. Chen Q-S, Prasad V, Chatterjee A (1999) Modeling of Fluid Flow and Heat Transfer in a Hydrothermal Crystal Growth System: Use of Fluid-Superposed Porous Layer Theory. J Heat Transfer 121:1049–1058
27. Chen Q-S, Prasad V, Chatterjee A, Larkin J (1999) A Porous Media-Based Transport Model for Hydrothermal Growth. J Crystal Growth 198/199:710–715
28. Kaldis E, Piechotka M (1994) Bulk Crystal Growth by Physical Vapor Transport, Hurle DTJ (ed) Handbook of Crystal Growth 2:615–658
29. Kaviany M (1995) Principles of Heat Transfer in Porous Media. Springer-Verlag, New York
30. Kansa EJ, Perlee HE, Chaiken RF (1977) Mathematical Model of Wood Pyrolysis Including Internal Forced Convection. Combus Flame 29:311–324
31. Bíró O, Preis K (1989) On the Use of the Magnetic Vector Potential in the Finite Element Analysis of Three-Dimensional Eddy Currents. IEEE Transactions on Magnetics 25:3145–3159
32. Kraus JD, Carver KR (1973) Electromagnetics. McGraw-Hill
33. Siegel R, Howell JR (1992) Thermal Radiation Heat Transfer. Hemisphere Publishing
34. Naraghi MHN, Chung BTF (1984) A Stochastic Approach for Analysis of Radiative Heat Transfer in Enclosures with Non-participating Media. J Heat Transfer 106:690–698
35. Naraghi MHN, Chung BTF, Litkouhi B (1988) A Continuous Exchange Factor Method for Radiative Exchange in Enclosures with Participating Media. J Heat Transfer 110:457–462
36. Nunes EM, Naraghi MHN (1998) Numerical Model for Radiative Heat Transfer Analysis in Arbitrarily Shaped Axisymmetric Enclosures with Gaseous Media. Num Heat Transfer A 33:495–513
37. Modest MF (1988) Radiative Shape Factors between Differential Ring Elements on Concentric Axisymmetric Bodies. AIAA J of Thermophysics and Heat Transfer 2:86–88

38. Drowart J, De Maria G (1960) Silicon Carbide. Pergamon, Oxford University Press
39. Kaneko T (1993) Growth Kinetics of Vapor-grown SiC. J Crystal Growth 128:354–357
40. Zhang H, Prasad V, Moallemi MK (1996) Numerical Algorithm Using Multizone Adaptive Grid Generation for Multiphase Transport Processes with Moving and Free Boundaries. Num Heat Transfer, Part B 29:399–421
41. Zhang H, Prasad V (2000) Modeling of High Pressure Liquid-encapsulated Czochralski Crystal Growth Processes. In: Szmyd JS, Suzuki K (eds) Modeling of Transport Phenomena in Crystal Growth. WIT Press 323–362
42. Balkas CM, Maltsev AA, Roth MD, Yushin NK (2000) Role of Temperature Gradient in Bulk Crystal Growth. Materials Science Forum 338–342:79–82
43. Anikin M, Madar R (1997) Temperature Gradient Controlled SiC Crystal Growth. Mater Sci and Eng B 46:278–286
44. Tairov YuM, Tsvetkov VF (1978) Investigation of Growth Processes of Ingots of Silicon Carbide Single Crystals. J Crystal Growth 43:209–212
45. Tairov YuM, Tsvetkov VF (1981) General Principles of Growing Large-size Single Crystals of Various Silicon Carbide Polytypes. J Crystal Growth 52:146–150
46. Nakata T, Koga K, Matsushita Y, Ueda Y, Niina T (1989) Single Crystal Growth of 6H-SiC by a Vacuum Sublimation Method, and Blue LEDs. In: Rahman MM, Yang CY-W, Harris GL (eds) Amorphous and Crystalline Silicon Carbide II. Springer Proc Phys 43:26
47. Syväjärvi M, Yakimova R, Kakanakova-Georgieva A, MacMillan MF, Janzén E (1999) Kinetics and Morphological Stability in Sublimation Growth of 6H and 4H SiC Epitaxial Layers. Mater Sci and Eng B 61–62:161–164
48. Lambropoulos JD (1987) The Isotropic Assumption During the Czochralski Growth of Single Semiconductors Crystals. J Crystal Growth 84:349–358
49. Fainberg J, Leister H-J (1996) Finite Volume Multigrid Solver for Thermo-elastic Stress Analysis in Anisotropic Materials. Comput Methods Appl Mech Engrg 137:167–174
50. Samant AV, Pirouz P (1998) Activation Parameters for Dislocation Glide in $\alpha$-SiC. Int J Ref Metals and Hard Materials 16:277–289